



Soft Matter

Geometry-controlled instabilities for soft-soft adhesive interfaces

Journal:	<i>Soft Matter</i>
Manuscript ID	SM-ART-06-2022-000808.R1
Article Type:	Paper
Date Submitted by the Author:	04-Oct-2022
Complete List of Authors:	Thomas, Elayne; University of Massachusetts Amherst, Polymer Science and Engineering Fu, Hongbo; University of Massachusetts Amherst, Polymer Science and Engineering Hayward, Ryan; University of Massaschusetts, Polymer Science and Engineering Crosby, Alfred; University of Massachusetts, Polymer Science and Engineering

SCHOLARONE™
Manuscripts

Geometry-controlled instabilities for soft-soft adhesive interfaces

Elayne M. Thomas, Hongbo Fu, Ryan C. Hayward, and Alfred J. Crosby

Abstract

Soft materials interfaces can develop complex morphologies, such as cavities or finger-like features, during separation as a result of a mechanical instability. While the onset and growth of these instabilities have been investigated previously for interfaces between rigid and soft materials, no existing predictive model provides insight for controlling the separation morphology associated with these instabilities when both “sides” of the interface are soft. Here, we expand previous models to account for the geometry and materials properties of two soft materials that form an interface. The total compliance of the system, which depends nonlinearly on the thickness of each contacting soft material, plays a primary role in governing the morphology of the separating interface. We validate this model with experimental measurements using a series of soft elastomers with varying layer thicknesses and fixed materials properties, in order to emphasize the geometry alone can give rise to the observed differences in the interface separation process. This model also demonstrates that the degree of geometric asymmetry, or the ratio of the layer thicknesses that form an interface, influences the stress experienced in either layer, thus providing a rich means of controlling how unstable interface separations develop and propagate. This framework is a powerful tool to understand and control adhesion mechanisms in fields ranging from biology to soft robotics, and provides intuition for engineering a separation mode for a desired end result.

Introduction

Many interfaces in biology and new technologies involve contact between two soft materials.¹⁻⁴ For these interfaces, it is often critical to control how they debond, or separate. For example, when high adhesion, or resistance to separation, is required, it is desirable to initiate the growth of cavities or finger-like protrusions. These processes often lead to the onset of fibril formation and other mechanisms that dissipate significant energy, hence enhancing adhesion performance. Alternatively, the onset of complex morphologies at soft materials interfaces can be undesirable for many applications, such as grip-and-release technologies in soft robotics. In these cases, uncontrolled interfacial morphologies may lead to the development of unpredictable stresses and unintended damage. While the control of interfacial separation processes and morphologies has been previously investigated for interfaces between a rigid and a soft material,⁵⁻⁷ similar studies on interfaces between two soft materials, or so-called soft-soft interfaces, have been limited.⁸ Accordingly, no model currently exists for guiding the design of soft-soft materials interfaces to achieve a desired separation process. Here, we build upon previous studies of rigid-soft interfaces to develop a new predictive model for soft-soft interfaces, and we validate this model with controlled experiments where materials properties are fixed and only the thickness of the interfacing soft layers is varied. These experiments, and the developed model, demonstrate that the thickness of both sides of a soft-soft interface can be used to control the interfacial separation morphology. This demonstration opens new opportunities for controlling the geometric symmetry of a soft-soft interface to inhibit the onset and growth of particular morphologies, which may help to prevent damage and extend lifetime performance for soft-soft interface technologies.

Previous studies of interfaces between rigid and soft materials have shown that cavities or finger-like defects develop when internal stresses during interfacial separation exceed stresses

along the edge of contact. The development of such morphologies is associated with the onset of elastic or viscous instabilities. A framework, based on treatment of the interfacial separation process as a fracture process,^{9,10} has been established to predict the materials properties and geometric conditions that lead to such instabilities for interfaces formed between rigid and soft interfaces.¹⁰⁰ In short, two dimensionless parameters govern these mechanisms. One parameter is the ratio between the contact length and the elasto-adhesion length scale. The contact length (a) is the lateral dimension that defines the extent of the interfacial area. The elasto-adhesion length scale is the ratio of the adhesion strength, G_c , or the critical energy release rate for interfacial separation, and the elastic modulus, E , for the soft material. The second dimensionless parameter is the ratio between the contact length and the thickness of the soft material, h . This ratio, a/h , is referred to as the degree of geometric confinement. As a/h increases, lateral strains cannot easily be accommodated within the elastic layer, which results in the development of elevated hydrostatic stresses during debonding and a higher probability of an instability in the bulk, such as fingering or cavitation.¹¹⁻¹⁴

This framework has provided clear guidelines for interface design when only one side of the interface is soft; however, design rules for two soft materials in contact are not clear using this formalism. Under these conditions, the geometric confinement of both "sides" of an interface can alter the separation process, which prohibits the definition of a single value of h . While notable previous work has considered the role of geometric confinement in soft-soft interfaces in controlling the wavelength, or dominant size scale, of complex separation processes for systems with $a/h \gg 1$,⁸ no existing model provides insight of whether an interface between two soft materials will or will not separate *via* an instability.

Here, we describe a formalism to determine the separation mode of two contacting soft materials, the thicknesses of which are denoted h_1 and h_2 , through an additive compliance model. In this model, the geometric confinement parameter of each layer contributes to the compliance of the bilayer independently, indicating that the total compliance can be tuned through the confinement of each layer separately. In addition, the separation mode map describing the (in)stability of the separating adhesive interface depends on both a/h_1 and a/h_2 , with the resulting mode ultimately governed by the most compliant layer. We find that predictions of compliance and separation mode to be in good agreement with experimental results of a model soft elastomer over a wide range of a/h_1 and a/h_2 whose observed delamination mode cannot be predicted by treating the thicknesses as additive. Our results carry significant implications to guide materials and device design for tunable adhesive performance and damage mitigation.

2 Results and Discussion

Section 2.1: A predictive model for soft-soft separation modes

To describe the adhesion of two soft layers at an interface and predict their separation mode, we extend an established formalism to predict how the properties of each layer influence the stability of interface separation.¹⁰ We focus on the geometry of an axisymmetric probe tack test, a common method for quantifying the energy per unit area required for interface separation, and define a as the radius of the contact interface between the soft axisymmetric probe and the soft substrate layer. Previous work has described the compliance (C) of a single elastic layer in contact with a rigid axisymmetric probe using correction factors that account for the geometric confinement parameter:^{15,16}

$$C = \frac{(1 - \nu^2)}{2Ea} \left[\left(1 + \frac{4}{3} \left(\frac{a}{h} \right) + \frac{4}{3} \left(\frac{a}{h} \right)^3 \right)^{-1} \right] \quad \text{Eq. 1}$$

where E and ν are the elastic modulus and Poisson's ratio of the elastic layer, respectively. The compliance is the rate of change in displacement per change in force at a fixed radius of contact. For the case of two compliant layers (referred to as "layer 1" and "layer 2") in contact, the total compliance takes into account the compliance of both soft layers independently:

$$C_s = \frac{(1-\nu^2)}{2Ea} \left[\left(1 + \frac{4}{3} \left(\frac{a}{h_1} \right) + \frac{4}{3} \left(\frac{a}{h_1} \right)^3 \right)^{-1} + \left(1 + \frac{4}{3} \left(\frac{a}{h_2} \right) + \frac{4}{3} \left(\frac{a}{h_2} \right)^3 \right)^{-1} \right] \quad \text{Eq. 2}$$

where h_1 and h_2 are the thicknesses of layer 1 and layer 2, respectively. In Eq. 2, the subscript s denotes 'soft-soft' interfaces; however, this equation is equivalent to Eq. 1 as a/h_1 or $a/h_2 \rightarrow \infty$ (i.e., if either layer thickness approaches zero). We also note that this analysis assumes that the elastic modulus of the soft-soft system is constant. With this definition of the compliance, we use fracture mechanics to develop an equation that defines a boundary between different modes of interfacial separation.

The rate at which elastic energy and mechanical work change as a function of area is known as the strain energy release rate, or simply the energy release rate, G . This parameter defines the driving force for interfacial crack propagation. The point at which it is energetically favorable for a crack to grow at the cost of making new surface area is defined as the critical energy release rate, also known as the fracture energy, G_c . For polymer interfaces, the critical energy release rate is dependent on the separation velocity^{5,9}; therefore, we define the zero-velocity G_c as G_0 . In this limit, interfacial separation thus occurs when $G > G_0$.

The energy release rate is determined from the compliance, force P , and a :

$$G = - \frac{(P' - P)^2 da}{4\pi a} \quad \text{Eq. 3}$$

where P' is the Hertzian force at a contact radius of a in the absence of adhesion. For contact between a flat probe and flat substrate, $P' = 0$, and $\sigma_{avg} = P / \pi a^2$ is the average stress. This

simplification is also valid for axisymmetric probe as $R \rightarrow \infty$. Substituting Eq. 2 into Eq. 3 yields an expanded expression of the driving force for edge crack propagation:

$$\frac{G_{edge}}{Ea} = \frac{9\pi}{128} \left(\frac{\sigma_{AVG}}{E} \right)^2 \left(\frac{0.75 + 2\left(\frac{a}{h_1}\right) + 4\left(\frac{a}{h_1}\right)^3}{\left\{0.75 + \frac{a}{h_1} + \left(\frac{a}{h_1}\right)^3\right\}^2} + \frac{0.75 + 2\left(\frac{a}{h_2}\right) + 4\left(\frac{a}{h_2}\right)^3}{\left\{0.75 + \frac{a}{h_2} + \left(\frac{a}{h_2}\right)^3\right\}^2} \right) \quad \text{Eq. 4}$$

If G_{edge} surpasses G_c , separation will initiate at the contact perimeter and propagate from the edge.^{10,15} However, if significant hydrostatic stresses develop before that criterion is reached, an instability is likely to drive interfacial separation. We set this criterion as when σ_{AVG}/E is greater than 1 to represent a the point above which a cavity is energetically driven to grow¹⁰; below this criterion, the lateral stress is released through crack growth along the edge of the contact perimeter.

Eq. 4 describes the boundary between stable and unstable separation modes and demonstrates that both elastic layers can be tuned independently, but act cooperatively, to determine the dominant debonding mode. We note that in the case of low adhesion or stiff materials, interfacial fingers or cavities will form that are independent of layer geometry, but depend on the geometry of defects at the interface.¹⁰ This deformation mode is outside of the scope of this paper, as geometric confinement is not the dominant factor in this separation mode.

The boundary described by Eq. 4 is a 3D surface with the confinement parameter of layer 1 and layer 2 contributing independently to the predicted separation mode, shown in **Figure 1a**. All soft-soft interfaces with values of a/h_1 , a/h_2 , and G_0/Ea that fall below the boundary should debond *via* edge crack propagation, while others will delaminate *via* an elastic instability. There are several attributes about this map that are important to note. The map is symmetric about the plane $a/h_1 = a/h_2$, indicating that for a given interface between soft materials, the geometric confinement of each layer is interchangeable to yield the same delamination mode. Secondly, the behavior of a hard/soft interface is recovered as either layer becomes infinitely thin (a/h_1 or a/h_2

$\rightarrow \infty$), consistent with Eq. 2. Thirdly, the model predicts an expansion in the edge crack propagation regime when both layers are unconfined (a/h_1 and a/h_2 are small), shown in yellow. This increase mathematically arises from the factor of 2 stemming from the use of two correction factors. Intuitively, this prediction can be rationalized by comparing the displacement required to create an interface with contact area A for a soft/hard system versus a soft/soft system. If both a/h_1 and a/h_2 are small in the latter case, less displacement is required of either layer to achieve the same contact radius, resulting in a reduced stress profile that is unattainable for the same material in a hard/soft system.

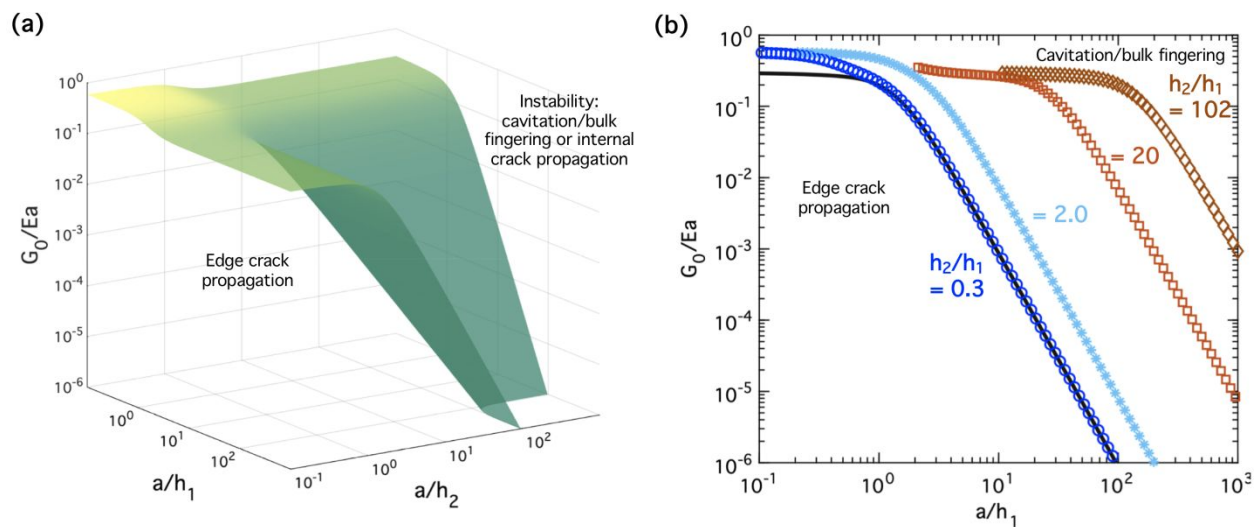


Figure 1: The separation mode map for soft on soft contact ($\sigma_{AVG}/E = 1$; $\nu = 0.5$). Accounting for confinement in both layer 1 (with thickness h_1) and layer 2 (with thickness h_2) expands the boundary between edge crack propagation and a bulk or interfacial stability from a line to a surface (a). 2D projections of the 3D separation mode map (b) show how the difference in confinement between two layers alters the region of stable delamination. Each curve delineates areas where an interface will separate *via* edge crack propagation (area under the curve) or through an instability (area above the curve). G_0 is the threshold energy required to initiate crack propagation.

The model also posits that a predicted separation mode is ultimately governed by the least confined layer, suggesting that a transition from an instability to a stable separation can only be achieved by adding a second layer that is sufficiently compliant. **Figure 1b** shows a 2D

representation of the separation mode map with traces of G_{edge}/Ea versus a/h_1 for varying thickness ratios, h_2/h_1 . In the 2D map, values of G_0/Ea , the lower limit of G_c/Ea , under the curve represent an edge crack propagation mode. The solid black line is equivalent to the hard on soft case where $a/h_2 \rightarrow \infty$. As h_2/h_1 increases, the boundary that separates stable and unstable debonding modes shifts to higher confinement regimes. This implies that for a constant a/h_1 , the additional compliance from the second layer increases the required stress to induce a bulk elastic instability, which shifts the criterion for cavitation or bulk fingering to a higher confinement parameter. However, simply adding a second soft layer does not necessarily shift the G_{edge}/Ea curve to higher values of confinement, as shown by the trace for $h_2/h_1 = 0.3$ (blue circles). In this case, G_{edge}/Ea is identical to that of a hard/soft interface above $a/h_1 \sim 1$, below which confinement has negligible impact on the mechanics of the interface. The insights from the additive compliance model for soft/soft adhesion are critical for designing soft interfaces, and these predictions could not be elucidated from considering only a rigid body in contact with an elastic layer.

Section 2.2: Tuning separation modes through geometry of PDMS soft contact pairs

Experiments to corroborate the predictions of our model were completed using an archetypal soft elastic system to observe a transition from unstable to stable interfacial separation. Polydimethylsiloxane (PDMS) was selected, and elastomer samples were synthesized by crosslinking a PDMS network (Sylgard 184 30:1 base to crosslinking agent by weight) blended with 30% weight fraction of linear PDMS ($M_w \sim 13.5$ kg/mol). The elastic modulus of the elastomer was $E = 27$ kPa, as measured from hard/soft contact adhesion tests. The rate-independent, elastic character of the network was confirmed by varying the rate of the contact

adhesion tests (**Figure S1a**) and by conducting a frequency sweep with a dynamic mechanical analyzer (DMA) (**Figure S1b**).

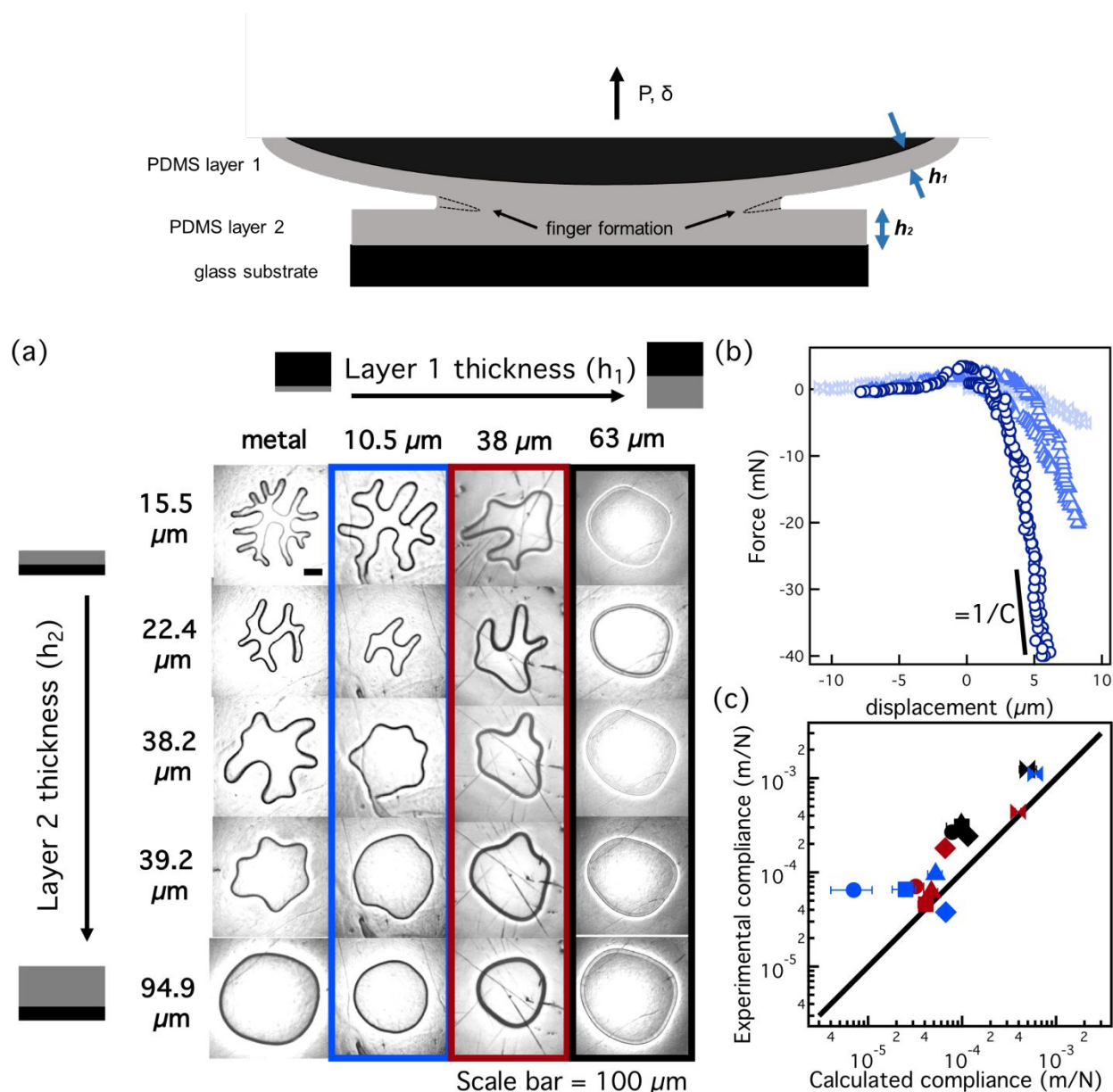


Figure 2: PDMS soft/soft adhesion measurements. The schematic illustrates the geometry for the sphere on flat soft/soft adhesion measurements ($R = 3.5$ mm). Bulk fingering is the primary instability observed during contact adhesion measurements. Three layer 1 films were measured with five layer 2 films to observe the transition from a bulk instability to an edge crack propagation (a). Decreasing the confinement ratio, a/h , of either layer 1 or layer 2 eventually leads to a stable edge crack separation mode. (b) Representative force-displacement curves for layer 1 = $10.5 \mu\text{m}$. Negative forces correspond to compressive forces and positive forces represent tensile forces. The compliance of the soft pair, measured as the inverse of the slope of the curve near the maximum compressive force, decreases as the thickness of layer 2 increases from $15.5 \mu\text{m}$ (o) to $38.2 \mu\text{m}$ (Δ) to $94.9 \mu\text{m}$ (\times). (c) Experimental compliance plotted against predicted compliance

from Equation 2, with the black line representing the line of unity. Error bars correspond to $\pm 2 \mu\text{m}$ for each layer thickness.

To compare the compliance, force capacity, and debonding stability of a soft/soft interface, three different “probe” (layer 1) thicknesses ($h_1 = 10.5 \mu\text{m} - 63 \mu\text{m}$) were tested against six different “substrate” (layer 2) thicknesses ($h_2 = 15.5 \mu\text{m} - 95 \mu\text{m}$) to vary the confinement parameters from ≈ 28 to 3.6. Films of PDMS were fabricated on glass using a doctor blade to vary the thickness; for the probe samples, the films were cast on polyacrylic acid-coated glass substrates and floated onto polished stainless steel hemispherical probes ($R = 3.5 \text{ mm}$). We reiterate here that the adhesion characteristics for a given contact pair is independent of how contact is made, such that layer 1 and layer 2 are interchangeable. The maximum contact radius is axisymmetric and was controlled to be similar for all soft pairs tested (Supplementary Information **Figure S2**). We observe a gradual transition from bulk fingering to edge crack growth upon decreasing the degree of geometric confinement in each elastic layer, signifying that the stability of the interface during separation is controlled by modifying the stress distribution in each layer.

Figure 2a shows the contact images at 70% of the maximum tensile strain captured during a contact adhesion measurement for each soft pair. Each column corresponds to a constant layer 1 thickness with varying a/h_2 , while each row corresponds to a constant layer 2 thickness with varying a/h_1 . The left-most column corresponds to contact adhesion measurements using a steel probe for each layer 2. For the hard/soft adhesion measurements, the delamination mode transforms from a bulk fingering with the thinnest PDMS film ($a/h_2 = 14$) to an edge crack growth for the thickest PDMS film ($a/h_2 = 3.6$). Previous work has shown that the wavelength of the fingering instability (l) scales with the thickness of the elastic layer such that $l = k \cdot h$, where k ranges from 2.5 – 3. This relationship is roughly consistent with our observations ($k = 3.5$, **Figure S3**). These instabilities remain when the hard probe is replaced with a second PDMS layer, shown

in the second column of **Figure 2a**, although the primary wavelength decreases for a given substrate. We expect that this observation is due to the reduced surface energy required to separate two PDMS surfaces compared to the PDMS/steel interface. Fingering instabilities persist until $h_1 = 63 \mu\text{m}$, where layer 1 is sufficiently compliant to allow edge crack growth. The trend is consistent with the force-displacement curves of the contact adhesion tests (**Figure 2b**), where the slope of the curve in compression decreases as either of the two layers becomes more compliant. Comparison between the theoretical compliance calculated from the additive compliance model and the experimental compliance attained from the force-displacement curves show good agreement in the range of compliances tested (**Figure 2c**), although the compliance of the stiffest materials approach the compliance of the instrument (10^{-5} m/N). These trends clearly reveal that geometry plays a powerful role in determining the separation mode of two soft materials in contact, and that the deformation mode can be tuned through the confinement of each layer independently.

Section 2.3: Experimental values of G_0/Ea corroborate predictions for the transition of separation modes from bulk fingering to edge crack propagation

The three-dimensional deformation mode map aligns with the experimentally-observed deformation modes, indicating that the confinement of each layer must be considered to accurately predict how the interface between two soft materials will separate. Values of G_0/Ea attained from contact adhesion tests (**Figure S5**) versus a/h_1 and a/h_2 for each soft contact pair on the 3D separation mode map show a clear transition from debonding *via* bulk fingering for highly confined layers to an edge crack propagation mode as a/h_1 and a/h_2 decrease (**Figure 3**). Two-dimensional projections are shown in **Figures 3a** and **3b**. We note that the set of points for $h_1 = 63 \mu\text{m}$ should clearly predict edge crack propagation from **Figure 2**, but are instead near the

boundary between edge crack and bulk instability (black points). This may be due the presence of less energetically stable defects where the driving force for an instability may be less than unity (here, we assumed $\sigma_{AVG}/E = 1$ as an approximate instability condition). Overall, the agreement between theoretical predictions and experimental results underscores the necessity of considering the geometric properties of both layers to understand how two soft materials debond.

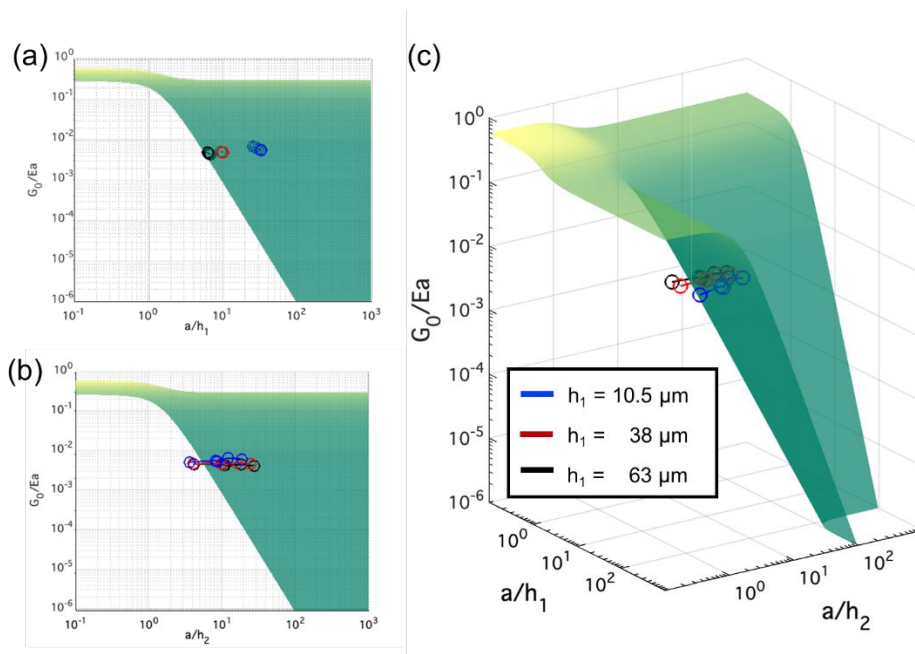


Figure 3: Superposition of experimental G_0/Ea values for PDMS soft-soft adhesion tests with the theoretical deformation mode map from the additive compliance model from perspectives of (a) layer 1, (b) layer 2, and (c) three-dimensional space. There is a clear transition between a bulk instability and stable separation mode that is in agreement with the delamination images in **Figure 2**.

Section 2.4: Effects of confinement asymmetry on the observed separation mode

A notable question is how the adhesion and separation process of a soft-soft interface changes if the confinement of the bilayer (a/h_T , where $h_T = h_{1+2}$) remains constant, but the distribution of material between layer 1 and layer 2 differs. Understanding how the symmetry of confinement impacts the separation mode is critical for designing stable soft materials interfaces, especially

with cost and material constraints. Here, we discuss theoretical and experimental insight into how confinement asymmetry may either be detrimental or beneficial for a stable separation mode.

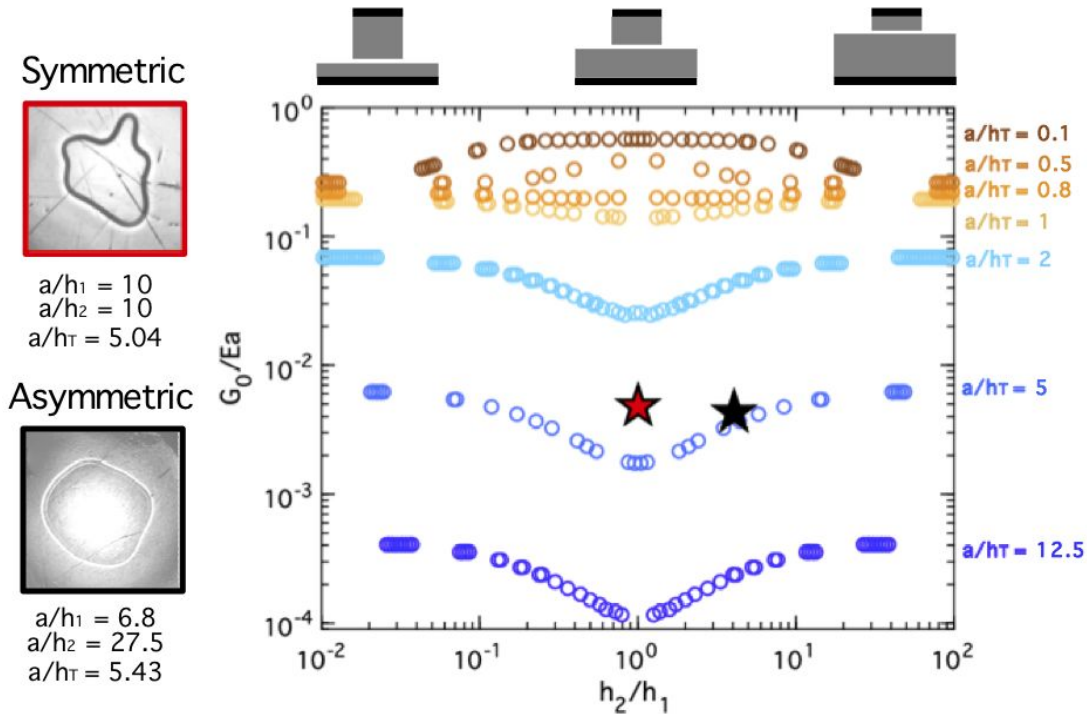


Figure 4. The role of asymmetry in adhesion of soft/soft interfaces. For each curve, the area above the line correlates to separation through an instability. Two soft contacts with the same total a/h_T can exhibit different modes of separation depending on how the stress distribution is shared between the two layers, as predicted by the model and observed experimentally. Stars correspond to G_0/Ea for each measurement on the left.

A soft/soft interface with a given a/h_T exhibits a local increase or decrease in the G_{edge}/Ea boundary near $h_2/h_1 = 1$, which arises from competing effects of confinement and stress distribution. **Figure 4** shows the normalized elasto-adhesive length for a family of traces over a range of a/h_T as a function of the thickness ratio h_2/h_1 . Extreme values of h_2/h_1 represent an asymmetric soft contact pair, while symmetric contact corresponds to $h_2/h_1 = 1$. The region below each curve indicates a stable mode of separation, while values of G_0/Ea above the curve results in an instability. For each a/h_T curve, we observe that G_{edge}/Ea is equivalent at both extremes of h_2/h_1 , since the adhesion behavior of a contact pair is independent of the position of layer 1 and 2. As

h_2/h_1 approaches unity, the values of G_{edge}/Ea delineating separation modes deviates from G_{edge}/Ea predicted at extreme values of h_2/h_1 . For $a/h_T > 1$, there is a local minimum in G_{edge}/Ea at $h_2/h_1 = 1$, meaning that interfacial separation has an increased probability of forming an instability for soft bilayers composed of symmetric layers. The opposite is true when $a/h_T < 1$, where G_{edge}/Ea exhibits a local maximum at $h_2/h_1 = 1$.

These findings are indicative of two different phenomena at play. When the layers are not geometrically confined, a symmetric pair minimizes the displacement in either individual layer compared to an asymmetric version with the same total thickness, which leads to a diminished stress distribution for the same contact radius. That still holds true at higher a/h_T , but the confinement effects overcome the benefit of reduced displacement. Through this analysis, we can define which effect dominates the boundary between edge crack propagation and cavitation/bulk fingering.

We confirm this symmetry argument by comparing two experimental results: $a/h_1:a/h_2 = 10:10$ and $6.8:27.5$. Both soft/soft pairs have a similar a/h_T (5.04 and 5.43, respectively); however, the distribution of PDMS for the latter pair is significantly more asymmetric than the former. As a result, 10:10 exhibits a fingering instability upon separation while 6.8:27.5 exhibits a uniform contact perimeter during debonding. Indeed, plotting the experimental G_0/Ea for the symmetric and asymmetric soft pair shows this to be the case, denoted by the stars in **Figure 4**.

Conclusions

We have presented a model that predicts the separation mode between two soft materials in contact, which requires accounting for confinement of each layer independently. By considering the compliance of each layer as additive, the separation mode map that describes how a soft materials

interface will separate arises from a combination of a/h_1 and a/h_2 . Through theoretical predictions and experimental results with a model elastomer, we find that the stability of contact during delamination is ultimately controlled by the most compliant layer, indicating that potential damage from unstable separation can be mitigated solely through modifying the geometry of a single layer. Further, analyzing how asymmetry in confinement affects the likelihood of a given separation mode reveals local extrema of G_{edge}/Ea for symmetric contact pairs ($h_2/h_1 = 1$), in agreement with experimental results of two contact pairs with the same a/h_T but different confinement asymmetry.

This framework is a powerful tool for understanding adhesion mechanisms in biology, soft robotics, medical devices, and other emerging technologies. For instance, the development of less destructive wound dressings by optimizing the adhesive geometry can result in accelerated healing times and reduced scarring. Soft devices designed to catch and release delicate organisms have been shown to reduce upregulation of stress responses in jellyfish,¹⁷ which has important implications for *in situ* measurements of other organisms that are endangered or are difficult to manipulate.¹⁸

More exploration is underway to apply this formalism to more non-ideal systems. In this work, we focused on a model elastic system where both materials had the same elastic modulus. While incorporating different elastic moduli into our framework is straightforward, fully describing adhesion of two soft materials with other differing properties such as viscoelasticity would pose a greater challenge. Future work will involve expanding out the additive compliance model to create a general framework that applies to films that are dissimilar in geometry as well as mechanical properties.

Conflicts of interest

There are no conflicts of interest to declare.

Acknowledgements

This work is supported by the U.S. Army Research Laboratory and the U.S. Army Research Office under contract/grant number W911NF-15-1-0538.

Experimental section

Materials: Poly(dimethyl siloxane) elastomer (PDMS) was prepared from a Sylgard™184 kit obtained from Dow Corning. Methyl-terminated linear PDMS (LPDMS) was obtained from Gelest (13.5 kg/mol) and used as received. Polyacrylic acid (PAA) was purchased from Sigma-Aldrich (1.8 kg/mol) and used as received. Cylindrical probes were purchased from McMaster-Carr (part number 91595A172) and smoothed with a polishing kit to an RMS roughness smaller than that of the cured elastomer layer. Glass substrates were purchased from University Wafer.

Elastomer preparation: The PDMS prepolymer and curing agent were first pre-mixed with a 30:1 ratio of prepolymer to curing agent by weight. The mixture was diluted to a weight fraction of 0.70 with LPDMS pre-cure to obtain the desired mechanical properties. The mixture was degassed for 30 minutes and cast onto glass substrates using a doctor blade to control the thickness. The formulations were cured for 48 hours at 70 °C. Thickness measurements were completed using the displacement actuator of the Contact Adhesion Tester, with approximate error of less than 1%.

Film transfer: A 3 wt% solution of PAA in deionized water was spun-cast onto UV-Ozone (UVO-Cleaner, Model 342, Jelight Company, Inc) cleaned glass substrates at 3000 rpm for 60 seconds to afford a 50 nm sacrificial layer. The PDMS mixture was cast onto the PAA-coated substrate and cured with the same conditions described above. The edges of the film were cut after crosslinking and floated onto RO water and transferred to a probe for adhesion measurements.

Dynamic mechanical analysis: Rheological measurements were measured by a dynamic mechanical analyzer (TA Instruments DMA 850) in a uniaxial tensile geometry. The elastomer was cut with a 6 mm biopsy punch with a thickness of 700 μm . A strain sweep was completed on the sample to confirm that measurements were taken in the linear elastic regime. Frequency sweeps were collected at 25 °C from 100 to 0.01 Hz at 0.5% strain with a 0.05 N preload.

Contact adhesion measurements: Contact adhesion tests were carried out on a custom-built instrument described in previous work.¹⁹ Briefly, displacement (δ) is controlled by a piezoelectric actuator (Burleigh Inchworm nanopositioner) and force (P) is measured using a capacitance-based load sensor (Physik Instrumente). A probe connected to a cantilever deflects when in contact with the substrate, which is converted into a force. The load cell and actuator are mounted over an inverted microscope (Zeiss Axiovert 200M). The cylindrical probes used had a diameter of 1 mm and radius of curvature (R) of 3.5 mm to create reproducible axisymmetric contact. The adhesion measurements were performed by bringing the probe into contact with a flat substrate at a displacement rate of 1 $\mu\text{m/s}$ until a maximum compressive preload and retracted until complete separation occurred. Force, displacement, and contact area images were continuously collected with a custom LabVIEW program during the experiment. Each experiment was cycled 3 times at the same location. From the experimental data, δ' and P' were calculated numerically with a

custom MATLAB code to determine G_0 and E , with more details in the Supplementary Information. Contact area was analyzed with ImageJ with an error less than 2%.

References

- 1 D. E. Discher, P. Janmey and Y. Wang, *Science*, 2005, **310**, 1139–1143.
- 2 S. R. Polio, A. N. Kundu, C. E. Dougan, N. P. Birch, D. E. Aurian-Blajeni, J. D. Schiffman, A. J. Crosby and S. R. Peyton, *PloS One*, 2018, **13**, e0204765.
- 3 B. T. Phillips, K. P. Becker, S. Kurumaya, K. C. Galloway, G. Whittredge, D. M. Vogt, C. B. Teeple, M. H. Rosen, V. A. Pieribone, D. F. Gruber and R. J. Wood, *Sci. Rep.*, 2018, **8**, 14779.
- 4 M. Cianchetti, C. Laschi, A. Menciassi and P. Dario, *Nat. Rev. Mater.*, 2018, **3**, 143–153.
- 5 A. N. Gent and S.-M. Lai, *J. Polym. Sci. Part B Polym. Phys.*, 1994, **32**, 1543–1555.
- 6 P. L. Drzal and K. R. Shull, *J. Adhes.*, 2005, **81**, 397–415.
- 7 J. Nase, O. Ramos, C. Creton and A. Lindner, *Eur. Phys. J. E*, 2013, **36**, 103.
- 8 J. Y. Chung, K. H. Kim, M. K. Chaudhury, J. Sarkar and A. Sharma, *Eur. Phys. J. E*, 2006, **20**, 47–53.
- 9 D. Maugis and M. Barquins, *J. Phys. Appl. Phys.*, 1978, **11**, 1989–2023.
- 10 A. J. Crosby, K. R. Shull, H. Lakrout and C. Creton, *J. Appl. Phys.*, 2000, **88**, 2956–2966.
- 11 H. Lakrout, P. Sergot and C. Creton, *J. Adhes.*, 1999, **69**, 307–359.
- 12 A. J. Crosby and K. R. Shull, *J. Polym. Sci. Part B Polym. Phys.*, 1999, **37**, 3455–3472.
- 13 K. R. Shull, C. M. Flanigan and A. J. Crosby, *Phys. Rev. Lett.*, 2000, **84**, 3057–3060.
- 14 A. N. Gent and C. Wang, *J. Mater. Sci.*, 1991, **26**, 3392–3395.
- 15 K. R. Shull, D. Ahn and C. L. Mowery, *Langmuir*, 1997, **13**, 1799–1804.
- 16 K. R. Shull, D. Ahn, W.-L. Chen, C. M. Flanigan and A. J. Crosby, *Macromol. Chem. Phys.*, 1998, **199**, 489–511.
- 17 M. Tessler, M. R. Brugler, J. A. Burns, N. R. Sinatra, D. M. Vogt, A. Varma, M. Xiao, R. J. Wood and D. F. Gruber, *Curr. Biol.*, 2020, **30**, R157–R158.
- 18 K. C. Galloway, K. P. Becker, B. Phillips, J. Kirby, S. Licht, D. Tchernov, R. J. Wood and D. F. Gruber, *Soft Robot.*, 2016, **3**, 23–33.
- 19 E. P. Chan, E. J. Smith, R. C. Hayward and A. J. Crosby, *Adv. Mater.*, 2008, **20**, 711–716.